Topological properties and dynamics of magnetic skyrmions

Naoto Nagaosa[1,2]* and Yoshinori Tokura[1,2]

Magnetic skyrmions are particle-like nanometre-sized spin textures of topological origin found in several magnetic materials, and are characterized by a long lifetime. Skyrmions have been observed both by means of neutron scattering in momentum space and microscopy techniques in real space, and their properties include novel Hall effects, current-driven motion with ultralow current density and multiferroic behaviour. These properties can be understood from a unified viewpoint, namely the emergent electromagnetism associated with the non-coplanar spin structure of skyrmions. From this description, potential applications of skyrmions as information carriers in magnetic information storage and processing devices are envisaged.

In classical mechanics, particles are represented by point masses or rigid bodies. In field theory, on the other hand, they are represented by wave-like excitations, akin to vibrations on a drumhead. In other words, they are excitations characterized by higher energy and momentum than the ground state (in this case the drumhead at rest), as well as a finite lifetime — the sound made by the drum decays after a certain time. In fact, explaining the stability of particles is a highly nontrivial issue. One possibility, originally proposed by Skyrme[1], is that the particles are topologically protected, in the sense that they are characterized by a topological integer that cannot be changed by a continuous deformation of the field configuration. This model — in which the particles are called skyrmions — has been proposed to explain hadrons in nuclear physics. Interestingly, however, it has also turned out to be relevant in condensed-matter systems such as the quantum Hall system[2], liquid crystals[3] and Bose condensate[4]. Indeed, it was predicted that topologically protected particles can be stabilized in chiral magnets[5–9] in the form of stable spin textures, referred to as magnetic skyrmions. Following these pioneering theoretical works, a flurry of recent experiments by neutron scattering[10], Lorentz transmission electron microscopy (LTEM)[11] and spin-resolved scanning tunnelling microscopy[12,13] have established the existence of skyrmion phases in magnets.

Figure 1a shows a schematic of a skyrmion configuration, with arrows depicting the direction of spin $\mathbf{n}(\mathbf{r})$ at spatial position $\mathbf{r} = (x,y)$. The spin at the core points down, while spins at the perimeter point up. The topological skyrmion number N_{sk} is defined as a measure of the wrapping of $\mathbf{n}(\mathbf{r})$ around a unit sphere[14,15] (see Box 1). As shown in Fig. 1g, there are several possible types of skyrmion structure[15,16] corresponding to different values of vorticity m and helicity γ, as defined in Box 1.

Various mechanisms can generate skyrmions in magnetic systems, and multiple mechanisms often contribute simultaneously. These are: (1) Long-ranged magnetic dipolar interactions. In magnetic thin films with perpendicular easy-axis anisotropy, the dipolar interaction favours an in-plane magnetization, whereas the anisotropy prefers an out-of-plane magnetization. The competition between these two interactions results in periodic stripes in which the magnetization rotates in the plane perpendicular to the thin film. An applied magnetic field perpendicular to the film turns the stripe state into a periodic array of magnetic bubbles or skyrmions[17–20]. (2) The relativistic Dzyaloshinskii–Moriya (DM) interaction[21,22]

in non-centrosymmetric magnets such as MnSi (refs 10,23–28), $Fe_{1-x}Co_xSi$ (refs 29–33), FeGe (refs 34–37) and $Mn_{1-x}Fe_xGe$ (ref. 38). In this case, an analogous transformation from the helical spiral into the triangular-lattice skyrmion crystal under an external magnetic field occurs. (3) Frustrated exchange interactions[39] or (4) four-spin exchange interactions[12], which can lead to atomic-sized skyrmion structures. Case (1) was extensively studied in the 1970s[18] aiming at applications for magnetic memory devices, while cases (2), (3) and (4) are a focus of intensive research now. Therefore, we remark here on some basic differences among these four cases. First, the size of the skyrmions is different. In case (1), skyrmions are typically of the order of 100 nm to 1 μm, which is comparable to the period λ of the spiral determined by the ratio of the dipolar and exchange interactions. In case (2) the size is determined by the DM interaction and is typically 5–100 nm. In cases (3) and (4), λ and the skyrmion size are of the order of the lattice constant (~1 nm). As a result, skyrmions and skyrmion crystals in cases (1) and (2) are larger than the lattice constant, and therefore the continuum approximation is justified. In these two cases, the energy density of the skyrmions is much smaller than the atomic exchange energy J, and the topological protectorate holds. In other words, discontinuous spin configurations — called monopoles — with energy of the order of J can create or annihilate the skyrmions. These large-scale skyrmions have many internal degrees of freedom, and hence are 'soft' and highly mobile, and free from the commensurability pinning by the crystal lattice.

Other important issues are γ and m. Depending on the mechanism of stabilization of the skyrmion, the dependence of γ and m on the energy differs (see Box 1). In case (1), the dipolar interaction is due to the magnetic charge $\rho_{mag} \propto \nabla \cdot \mathbf{n}$. To suppress ρ_{mag} and the associated energy cost, $m = 1$ and $\gamma = \pm\pi/2$ are required, and when m and γ do not take these values the energy cost is higher. However, the sign of $\gamma = \pm\pi/2$ remains undetermined endowing the skyrmion with helicity degrees of freedom. In case (2), the energy for skyrmion formation is lowest for $m = 1$ and $\gamma = \pm\pi/2$, but the sign of γ is determined by the sign of the DM interaction, D, which in turn is determined by the chiral crystal structure. In the cases of the frustrated exchange interaction (3) or four-spin interaction (4), the energies of skyrmions and anti-skyrmions, that is, energies for values of $m = \pm1$, are degenerate, and γ can take an arbitrary value.

Some remarks are in order regarding the topological nature of magnetic bubbles, which have been extensively studied for

[1]RIKEN Center for Emergent Matter Science (CEMS), Wako 351-0198, Japan, [2]Department of Applied Physics, The University of Tokyo, Tokyo 113-8656, Japan. *e-mail: nagaosa@riken.jp
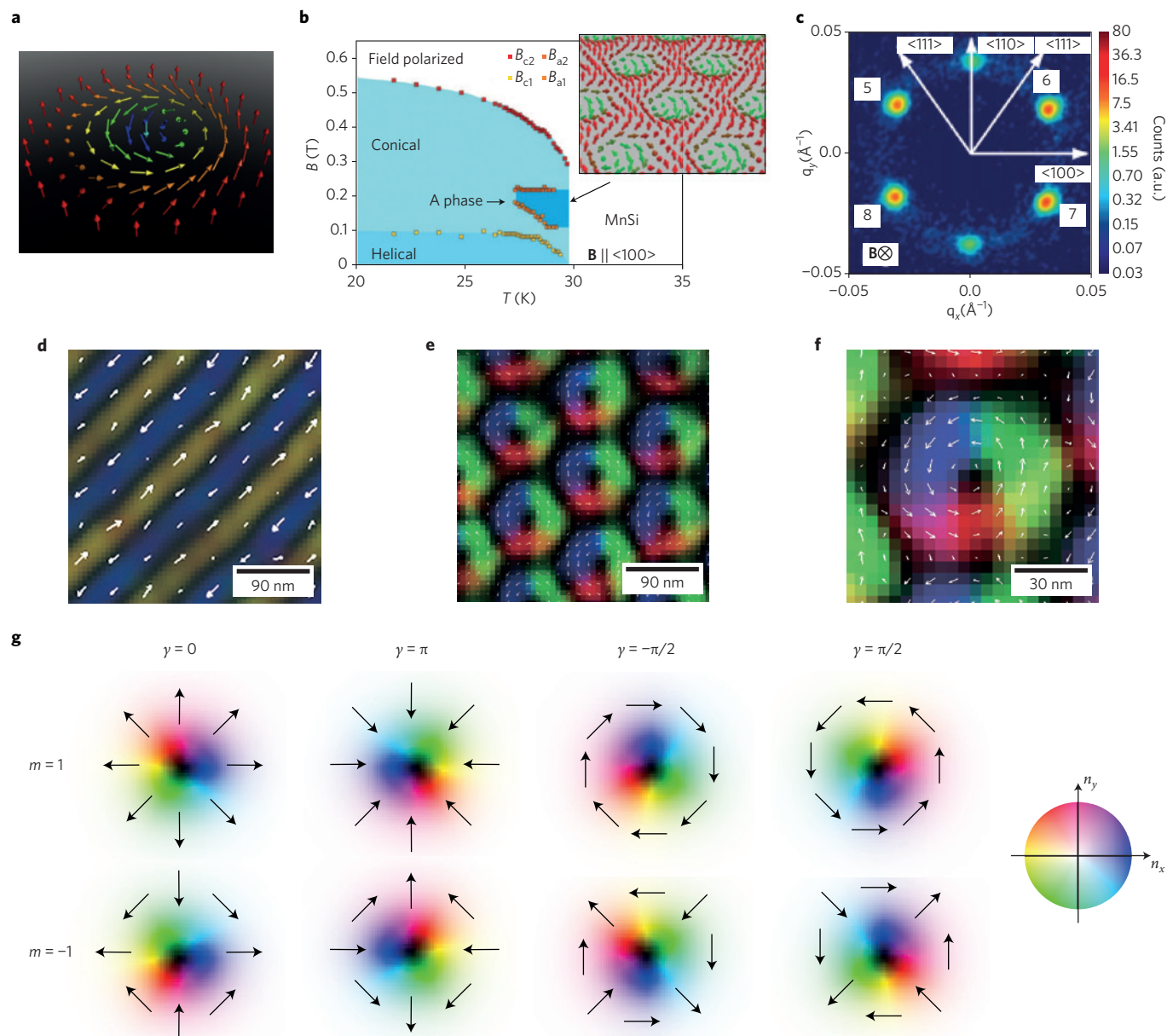
Figure 1 | The skyrmion spin structures. a, A schematic of the spin configuration of a single skyrmion. The arrows indicate the direction of the spins, and their colours represent the normal component to the plane, that is, from up direction (red) to the down direction (blue). **b**, The phase diagram of MnSi as a function of T and B. Inset: A schematic view of the triangular crystal of skyrmions, corresponding to the A phase. B_{a1}, B_{a2}, B_{c1} and B_{c2} are the critical values of the magnetic field on the phase boundaries. **c**, The Bragg spots in momentum space corresponding to the skyrmion crystal observed by SANS. **d–f**, Real-space observation of the helix state (**d**) and skyrmion crystal state (**e**) imaged by LTEM. In **f**, a magnified skyrmion from **e** is shown. The colour (brightness) corresponds to the direction (magnitude) of the in-plane component of the spins as shown in **f**. The black colour means the spins are pointing either up or down with a zero in-plane component. **g**, Skyrmion structures with varying m and γ. The arrows indicate the direction of the in-plane spin component, and the brightness indicates the normal component to the plane, with white denoting the up direction and black the down direction. All the structures of the anti-skyrmions ($m = -1$) are equivalent on rotation in the x–y plane. The relative stability of each structure is determined by the mechanism or interaction generating the skyrmion. Figure reproduced with permission from: **b,c**, ref. 10, © 2009 AAAS; **d–f**, ref. 11, © 2010 NPG.

applications in magnetic memories[18,40], with a focus on the z component of the magnetization[19]. When considering also the in-plane components, some magnetic bubbles are equivalent to skyrmions, whereas others are topologically trivial. As discussed above, the size of the magnetic bubble due to dipolar interactions (case 1) is 100 nm to 1 μm, whereas that of a skyrmion with a DM interaction (case 2) is 5–100 nm; the size directly determines the ultimate memory density. Regarding helicity degrees of freedom, magnetic bubbles have much richer structures, and often take on complex stripy patterns[41,42]. The case of skyrmions and bubbles differs also in

terms of the preferred excitation to drive the motion of the magnetic structures, which is an external magnetic field in the case of bubbles, whereas skyrmions are often coupled to the conduction electrons and can be driven by a very low current density[43,44] (see section 'Dynamics of skyrmions').

Skyrmions exhibit a variety of unique topological phenomena, which can be described by the emergent electromagnetic field (EEMF)[45–47], associated with the spin configuration (they are defined in the section 'Dynamics of skyrmions' and in Box 1). An example is the topological Hall effect induced by the emergent

Box 1 | Topological properties.

The skyrmion number

The swirling structure of a skyrmion is characterized by the topological skyrmion number defined by

$$N_{sk} = \frac{1}{4\pi} \iint d^2 \mathbf{r} \, \mathbf{n} \cdot \left(\frac{\partial \mathbf{n}}{\partial x} \times \frac{\partial \mathbf{n}}{\partial y} \right) \qquad (B1)$$

as the integral of the solid angle, and counts how many times $\mathbf{n}(\mathbf{r}) = \mathbf{n}(x,y)$ wraps the unit sphere[14,15]. Using the symmetry of the skyrmion, one can write

$$\mathbf{n}(\mathbf{r}) = (\cos\Phi(\varphi)\sin\Theta(r), \sin\Phi(\varphi)\sin\Theta(r), \cos\Theta(r)) \qquad (B2)$$

where we introduce the polar coordinates $\mathbf{r} = (r\cos\varphi, r\sin\varphi)$. Putting this form into equation (B1), we obtain

$$N_{sk} = \frac{1}{4\pi} \int_0^\infty dr \int_0^{2\pi} d\varphi \, \frac{d\Theta(r)}{dr} \frac{d\Phi(\varphi)}{d\varphi} \sin\Theta(r) = [\cos\Theta(r)]_{r=0}^{r=\infty} [\Phi(\varphi)]_{\varphi=0}^{\varphi=2\pi}$$

Accordingly, one can classify the skyrmion structures as follows. Suppose the spins point up at $r \to \infty$ while they point down at $r = 0$. Then, $[\cos\Theta(r)]_{r=0}^{r=\infty} = 2$. Now, there are several possibilities for $\Phi(\varphi)$. The vorticity is defined by the integer $m = [\Phi(\varphi)]_{\varphi=0}^{\varphi=2\pi}/2\pi$. Therefore, the vorticity determines the skyrmion number as $N_{sk} = m$, once the boundary condition at $r \to \infty$ is fixed. We further define the helicity by the phase γ appearing in

$$\Phi(\varphi) = m\varphi + \gamma \qquad (B3)$$

We show in Fig. 1g various skyrmion structures corresponding to vorticity $m = \pm 1$, and $\gamma = 0$, $\pm\pi/2$ and π, Fig. 1a corresponds to $m = 1$ and $\gamma = \pi/2$.

From equations (B2) and (B3), the magnetic charge $\rho_{mag} = \nabla \cdot \mathbf{n}$ is calculated as

$$\rho_{mag} = \cos[(m-1)\varphi + \gamma]\left(\frac{d\Theta}{dr} \cos\Theta + \frac{m}{r} \sin\Theta \right)$$

On the other hand, the DM interaction is given by

$$H_{DM} = D\mathbf{n} \cdot (\nabla \times \mathbf{n}) = D\sin[(m-1)\varphi + \gamma]\left(\frac{d\Theta}{dr} + \frac{m}{2r} \sin2\Theta \right)$$

or

$$H_{DM} = D\mathbf{n} \cdot (\mathbf{e}_z \times \nabla)\mathbf{n} = D\sin[(m-1)\varphi + \gamma]\left(\frac{d\Theta}{dr} + \frac{m}{2r} \sin2\Theta \right)$$

Therefore, the state with vorticity $m = +1$ and $\gamma = \pm\pi/2$ has the lowest energy, where the sign of γ is determined by the sign of D, which in turn is determined by the crystal structure. (When the DM vector is rotated by $\pm\pi/2$, $\gamma = 0$ or π becomes the stable configuration[109].)

In the case of the four-spin interaction (case 3) or the frustrated exchange interaction (case 4), there is no distinction between the skyrmion and anti-skyrmion, that is, $m = \pm 1$ and γ can take an arbitrary value.

Emergent electromagnetic field

One can describe the interaction between the spin textures and the conduction electrons in terms of the EEMF expressed by the spin directions. We consider the double-exchange model where the conduction electrons and spins are coupled ferromagnetically at each site by Hund's rule coupling. In the strong coupling limit, the spin wavefunction $|\chi(\mathbf{r})>$ of the conduction electron at $\mathbf{r}$ corresponding to the localized spin $\mathbf{n}(\mathbf{r})$ in equation (B2) is given by

$$|\chi(\mathbf{r})> = \left(\cos\frac{\Theta(\mathbf{r})}{2}, \, e^{i\Phi(\mathbf{r})} \sin\frac{\Theta(\mathbf{r})}{2} \right)^T$$

where ^{T} means the transpose. Therefore, when a conduction electron hops between two sites $\mathbf{r}$ and $\mathbf{r} + c\boldsymbol{\eta}_\alpha$ ($\boldsymbol{\eta}_\alpha$ is the unit vector along $\alpha(=x,y,z)$ direction, α is the space index and c a lattice constant), the matrix element is given by

$$t_\delta(\mathbf{r}) = t <\chi(\mathbf{r}) \,|\, \chi(\mathbf{r} + c\boldsymbol{\eta}_\alpha)>$$

where t is the original transfer integral of the conduction electron. $t_\alpha(\mathbf{r})$ is in general a complex number, and can be written as $t_\alpha(\mathbf{r}) = |t_\alpha(\mathbf{r})|e^{ica_\alpha(\mathbf{r})}$. This phase factor $e^{ica_\alpha(\mathbf{r})}$ is analogous to the Peierls factor in the presence of the external magnetic field and hence we can regard $a_\alpha(\mathbf{r})$ as the vector potential of an effective electromagnetic field. Assuming the slowly varying spin configuration over the lattice constant c, we obtain $a_\alpha(\mathbf{r}) = -i<\chi(\mathbf{r}) \,|\, \partial_\alpha\chi(\mathbf{r})> = \frac{1}{2}\partial_\alpha\Phi(1 - \cos\Theta)$. From this expression, one can easily confirm that the emergent magnetic field b_z is related to the solid angle as

$$b_z = \frac{\partial a_y}{\partial x} - \frac{\partial a_x}{\partial y} = \frac{1}{2}\mathbf{n} \cdot \left(\frac{\partial \mathbf{n}}{\partial x} \times \frac{\partial \mathbf{n}}{\partial y} \right)$$

Therefore, the total emergent magnetic flux associated with a skyrmion is $2\pi N_{sk}$. These considerations can be easily generalized to the three-dimensional case and also to the emergent electric field e_α as

$$b_\alpha = \frac{1}{2}\varepsilon^{\alpha\beta\gamma}\mathbf{n} \cdot (\partial_\beta\mathbf{n} \times \partial_\gamma\mathbf{n}) \qquad (B4a)$$

$$e_\alpha = \mathbf{n} \cdot (\partial_\alpha\mathbf{n} \times \partial_t\mathbf{n}) \qquad (B4b)$$

where $\partial_\mu = \partial/\partial x_\mu$, $\varepsilon^{\alpha\beta\gamma}$ is the totally antisymmetric tensor in three dimensions, and the coupling to the conduction electrons is described by the Lagrangian

$$L_{int} = j_\mu a_\mu \qquad (B5)$$

with j_μ being the density and current density of conduction electrons as in the case of the Maxwell electromagnetic field A_μ. Here μ is the space–time index.

We mention here that the well-known spin-transfer torque arises from equation (B5). Namely, the variation of a_μ with respect to $\mathbf{n}$ is given by

$$\delta a_\mu = -\frac{1}{2}\delta\mathbf{n} \cdot (\mathbf{n} \times \partial_\mu\mathbf{n}) \qquad (B6)$$

Combined with the variation of the Berry phase term ω as $\delta\omega = -\frac{1}{2}\delta\mathbf{n} \cdot (\mathbf{n} \times \partial_t\mathbf{n})$, equation (B6) leads to the equation of motion as

$$[\partial_t + (\mathbf{j} \cdot \nabla)]\mathbf{n}(\mathbf{r},t) = 0$$

which describes the current-driven motion of the spin texture with spatially varying $\mathbf{n}$.

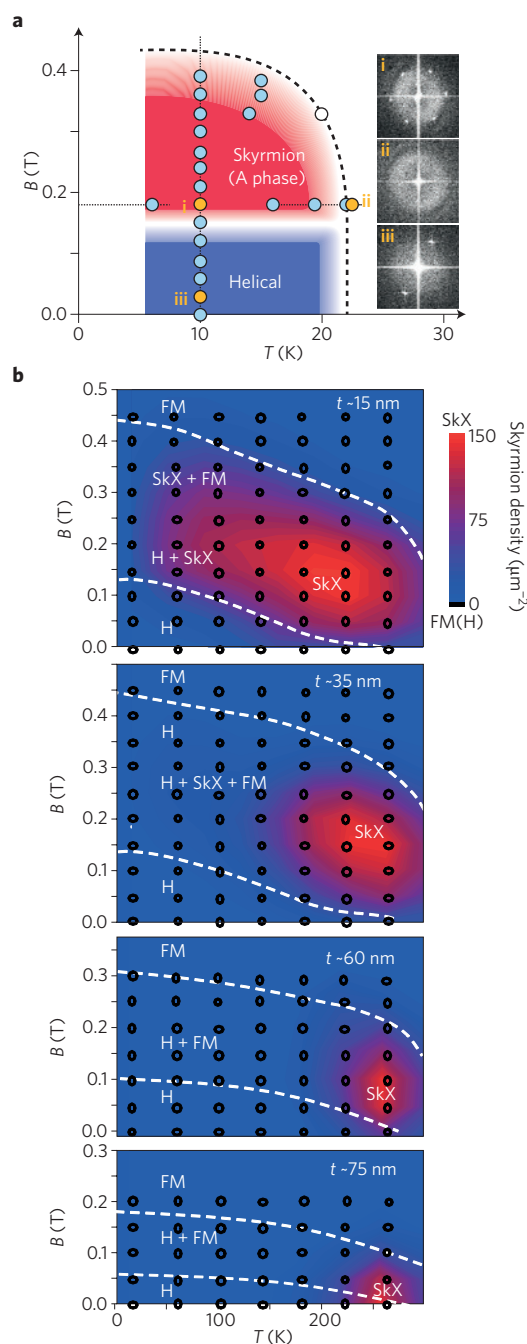**Figure 2 | Phase diagrams of thin-film samples of chiral magnets as a function of magnetic field and temperature. a**, Phase diagram of a MnSi thin film with a thickness of ~50 nm obtained from the patterns in the diffractographs shown in the insets i, ii and iii, which correspond to skyrmion, disordered and helical phases, respectively. The blue dots show (*T*,*B*) points where diffractographs were actually taken, and the orange dots correspond to those whose diffractograms are shown in the inset. **b**, The dependence of the SkX phase diagram for FeGe on the sample thickness (*t*). H, helical state; FM, ferromagnetic state. The colour scale indicates the skyrmion density per square micrometre. Figure reproduced with permission from: **a**, ref. 85, © 2012 ACS; **b**, ref. 36, © 2011 NPG.

magnetic field of the skyrmions on conduction electrons, which has been experimentally observed[48–53]. The motion of the skyrmions leads to the temporal change of the emergent magnetic field and hence to an electromagnetic induction. The induced emergent electric field contributes to the Hall effect when the skyrmions begin

to move[52]. This has been observed recently[54], demonstrating the physical reality of the EEMF in solids. In the following sections we will review these recent experimental and theoretical developments from the unified viewpoint of topology and the EEMF.

Observation of skyrmions in chiral-lattice magnets

Among many possible skyrmion-hosting materials are the cubic but non-centrosymmetric magnets, where non-collinear spin configurations — including screw spin (single-**q**) and skyrmion (multiple-**q**) states — can occur. The antisymmetric DM interaction results in the helical spin configuration as described by the Hamiltonian in the continuum approximation[55,56]

$$H = \int dr \left[\frac{J}{2} (\nabla \mathbf{n})^2 + D\mathbf{n} \cdot (\nabla \times \mathbf{n}) - \mathbf{B} \cdot \mathbf{n} \right] \quad (1)$$

where **B** is the magnetic field. The ground state of the Hamiltonian in equation (1) is a helical state with a single wavevector **Q** whose magnitude $Q = 2\pi/\lambda$ is fixed to be D/J, while its direction is variable. When D/J is small, the continuum approximation is justified, and the spin plane is perpendicular to **Q** to minimize the energy in equation (1). MnSi with the B20-type structure is an example of this helical magnet with $|\mathbf{Q}| = 0.043$ Å^{-1} ($\lambda = 18$ nm), which shows a novel temperature (*T*)–pressure phase diagram[23–28,57–65]. Neutron scattering experiments on MnSi (ref. 10) and Fe$_{1-x}$Co$_x$Si (refs 31,32) have identified the phase hitherto known as the 'A phase'[66] (shown in Fig. 1b) with a two-dimensional skyrmion crystal (SkX) phase. Theoretical analysis concludes that the SkX is stabilized by thermal fluctuations above the conical state in a limited region near the transition temperature, while the conical state with the wavevector **Q** parallel to the magnetic field is more stable in the rest of the phase diagram[10]. This type of SkX phase can be viewed as the hybridized triple-**q** state, in which **n**(**r**) can be expressed as

$$\mathbf{n}(\mathbf{r}) \approx \mathbf{n}_{\text{uniform}} + \sum_{i=1}^{3} \mathbf{n}_{\mathbf{Q}_i}(\mathbf{r} + \Delta \mathbf{r}_i)$$

Here, $\mathbf{n}_{\mathbf{Q}_i}(\mathbf{r}) = A[\mathbf{n}_{i1}\cos(\mathbf{Q}_i \cdot \mathbf{r}) + \mathbf{n}_{i2}\sin(\mathbf{Q}_i \cdot \mathbf{r})]$, and $\mathbf{Q}_i \cdot \Delta \mathbf{r}_i$ is the phase of each screw component, *A* is the magnetization of a single helix with the **q**-vector $\mathbf{Q}_i$, and $\mathbf{n}_{\text{uniform}}$ is the uniform magnetization induced by the Zeeman effect. The three **q**-vectors are all normal to the applied magnetic field direction, forming an angle of 120° with each other, and satisfying the relation

$$\sum_{i=1}^{3} \mathbf{Q}_i = 0$$

When one skyrmion is singled out from this hexagonal SkX state, it corresponds to the case $m = 1$, $\gamma = \pi/2$ shown in Fig. 1g. The magnetic helicity of the skyrmion depends on the sign of the DM interaction, as well as that of the screw state.

The SkX can be observed in terms of the magnetic scattering of neutrons (and possibly of X-rays). Reflecting the large length-scale of the SkX compared with the lattice spacing, small-angle neutron scattering (SANS) is employed[10,31,32,34,37,58,62,63,67–76]. The reciprocal-space SANS patterns for the SkX on the plane normal to the incident neutron **k**-vector shows up as a hexagon with the norm of $|\mathbf{Q}|$, that is, Fourier transform of the two-dimensional hexagonal SkX lattice as shown in Fig.1c (ref. 10), whereas the conical spin phase with the wavevector parallel to the magnetic field generates no pattern on this plane. A similar observation of the SkX will be possible with use of resonant soft X-ray scattering with the advantage of being applicable to crystals of reduced size or thin films; this remains an ongoing experimental effort.

For the real-space observation of SkX and also individual/isolated skyrmions at the nanometre scale, various electron and

scanning probe microscopy techniques may be employed. Examples include the recent application of magnetic force microscopy for the observation of a skyrmion crystal on the surface of a bulk crystal[77] and spin-polarized scanning tunnelling microscopy on ultrathin magnetic thin films[78,79]. Furthermore, various spin-polarized electron microscopy techniques[80] may be used for the observation of skyrmion crystals and single skyrmions. One important condition for such observations is, however, the necessity of an external magnetic field, which limits the use of some electron microscopy tools. In this context, LTEM is a powerful method that has nanometric spatial resolution and allows the application of a vertical magnetic field[81-86]. It can be used to observe the in-plane magnetization M of a plate-like specimen of thickness of less than 100 nm, through which the electron beam can transmit. Lorentz transmission electron microscopy makes use of the generated in-plane B field arising from the in-plane M, which generates the Lorentz force on the incoming electrons. The deflected electrons from regions with different in-plane M show interference patterns at under-focused and over-focused positions. For example, magnetic domain walls appear as bright or dark lines in the defocused position[80,82], whereas the proper screw state exhibits a striped contrast[84]. By analysing the two patterns in terms of the transport-of-intensity equation method[83], the local in-plane M distribution can be visualized with a spatial resolution of a few nanometres. Lorentz transmission electron microscopy can work well for the real-space observation of skyrmions or SkX with a size of more than a few nanometres, not only in B20-type helimagnets but also in many chiral or achiral magnets, corresponding to cases (1) to (3) described earlier. In a two-dimensional model of helical magnets, the skyrmion crystal state is stable over a wide range of T and B compared with the conical state when the magnetic field is perpendicular to the plane[87-89]. In the context of the formation of stable skyrmions in the thin-plate crystal used in LTEM measurements, it has been theoretically discussed that the uniaxial anisotropy[90-93] or the inhomogeneous chiral modulations across the layer thickness[94] stabilizes the skyrmion phase over the conical state. The importance of the combination of the DM and dipolar interactions has also been discussed[95].

We exemplify the two topological spin textures observed for a (001) thin plate of $Fe_{0.5}Co_{0.5}Si$ with B20-type chiral crystal structure (space group $P2_13$)[11]. The LTEM observation of the state below the magnetic transition temperature (~40 K) at zero magnetic field reveals the stripy pattern (Fig. 1d) of the lateral component of M with a period of $\lambda = 90$ nm; this corresponds to the proper screw spin structure propagating along [100] or [010]. When a magnetic field of 50 mT is applied perpendicular to the film, a two-dimensional SkX as described above is observed in real space (Fig. 1e). A hexagonal lattice is formed by periodic arrays of spin-swirling structures (Fig. 1f) and the lattice spacing (a_s) is identical to $2/\sqrt{3}$ of the stripe period λ ($\lambda = 90$ nm). The helicity in each skyrmion reflects the sign of the DM interaction of this compound, hence indicating the uniformity of the chiral domain of the crystal structure. When crystal domains with different chirality are observed, the skyrmion helicity can be reversed[96]. Although LTEM cannot specify the direction of the magnetization perpendicular to the film, it is possible to retrieve such information by knowing the direction of the external magnetic field. With the external field applied downward, the black background (that is, zero lateral component) can be assigned to the upward direction of spins whereas the black cores can be assigned to the downward direction.

The experimental phase diagrams for the SkX were obtained on the basis of such real-space observations by LTEM. Some results on thin plates of MnSi (ref. 85) and FeGe (ref. 36) are summarized in Fig. 2a,b. In Fig. 2b, the phase change of the spin texture in FeGe is represented as contour maps of skyrmion density. As compared with the bulk (Fig. 1b), the SkX phase in thin films extends over a wider region in the $T–B$ plane, surrounded by the screw (conical)

Table 1 | List of transition temperatures (T_N) and helical periods (λ) of helimagnets.

Material		T_N (K)	λ (nm)	Reference
MnSi	Bulk	30	18	23
	Epitaxial thin film	45	8.5	51
$Mn_{1-x}Fe_xSi$	$x = 0.06$	16.5	12.5	25
	$x = 0.08$	10.6	11	25
	$x = 0.10$	6.8	10	25
$Fe_{1-x}Co_xSi$	$x = 0.10$	11	43	29,33
	$x = 0.5$	36	90	29,33
	$x = 0.6$	24	174	29,33
	$x = 0.7$	7	230	29,33
MnGe	$T = 20$ K	170	3	50
	$T = 100$ K	-	3.4	50
	$T = 150$ K	-	5.5	50
$Mn_{1-x}Fe_xGe$	$x = 0.35$	150	4.7	38
	$x = 0.5$	185	14.5	38
	$x = 0.7$	210	77	38
	$x = 0.84$	220	220	38
FeGe	Bulk	278	70	34
Cu_2OSeO_3	Bulk	59	62	76
	Thinned plate	-	50	86

and collinear (ferromagnetic) spin sates. In thin (<100 nm) films of MnSi and $Fe_{1-x}Co_xSi$, the SkX phase under an intermediate field remains stable even at the lowest temperatures. The increasing stability of the SkX phase compared with the conical phase with decreasing film thickness is clearly discerned in Fig. 2b for the SkX phase of FeGe ($a_s = (2/\sqrt{3}) \times 70$ nm). This is because the spins cannot complete the spiral along the magnetic field and/or because the magnetic anisotropy is changed when the thickness of the thin film becomes the order of, or smaller than, λ (refs 87–95).

Skyrmions in different magnetic systems

Helimagnets with high symmetry but chiral crystal structures such as the cubic B20-type ($P2_13$) compounds are likely to host the skyrmion phase either in the presence of an applied magnetic field or when the material is in a thin-film form. (See Table 1 for the list of materials.) The validity of the effective spin Hamiltonian approach (for example, equation (1)) to the chiral-lattice magnet has been demonstrated also for the insulating magnet Cu_2OSeO_3 with the same space group $P2_13$ as the B20 compounds (but with a different atomic arrangement)[86]. In this material, the unit cell is composed of four inequivalent Cu sites; three Cu spins align approximately parallel and one spin antiparallel, forming a locally ferrimagnetic state[97]. In reality, due to the DM interaction arising from the chiral lattice structure, the coarse-grained local magnetization is gradually twisted to form a proper screw state with a period λ of 50 nm. In spite of the absence of the conduction electrons, the insulating helimagnet Cu_2OSeO_3 shows an analogous magnetic phase diagram in the $T–B$ plane to those of metallic B20-type (for example, MnSi) compounds; the SkX phase in bulk is also confirmed to exist in a narrow $T–B$ window near the phase boundary with the paramagnetic state by SANS experiments, as well as by magnetization measurements[69,76,86]. Again, the LTEM observation indicates that the hexagonal-lattice SkX phase expands to a broad $T–B$ region in the thin (~50 nm) film specimen, analogous to the results shown in Fig. 2.

An important point to note here is that the insulating chiral-lattice magnet is multiferroic. In multiferroics, the ferroelectric and
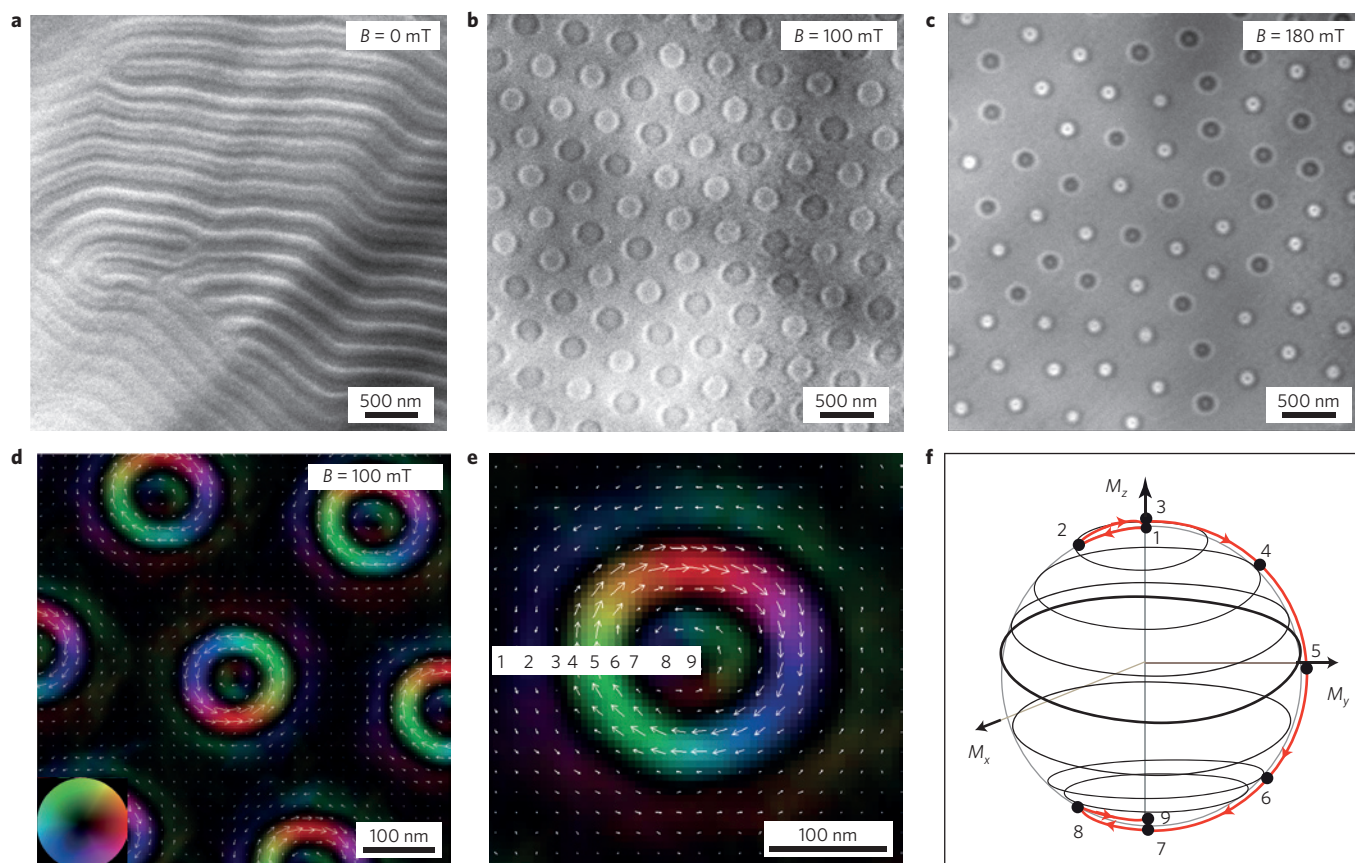
Figure 3 | Various spin textures in dipolar-driven skyrmion systems. a–c, TEM images of a (001) Sc-doped barium ferrite thin film. **a**, The striped domains at zero field. **b**, The triangular skyrmion lattice in a 100-mT field. Bright and dark colours correspond to the two helicities $\gamma = \pm\pi/2$ of skyrmions, which are randomly distributed even though the positions of skyrmions are ordered. **c**, By increasing the magnetic field to 180 mT, the size of skyrmions is reduced. **d**, Lorentz microscope image of the triangular lattice of skyrmions with the triple-ring structure and random helicities. Colour wheel and white arrows indicate the magnitude and direction of the in-plane magnetization. **e**, Close up of a skyrmion. **f**, Mapping of spin direction in the skyrmion to the M_x–M_y–M_z sphere. Numbers 1–9 correspond to the distance from the core shown in **e**. The direction of the spin rotation goes back and forth corresponding to the helicity degrees of freedom. Figure reproduced from ref. 41, © 2012 NAS.

magnetic orders coexist[98–102]. In chiral-lattice magnets, in general, the chemical bond, for example, the hybridization between magnetic d-orbital and ligand p-orbital states, is modulated by the spin–orbit interaction when the compound exhibits ferromagnetic or related orders, thereby producing a macroscopic electric polarization (P)[102]. In the case of Cu_2OSeO_3 with space group $P2_13$, for example, symmetry considerations predict that $P = 0$ for $M \parallel [001]$, while non-zero $P \parallel [001]$ for $M \parallel [110]$, and non-zero $P \parallel [111]$ for $M \parallel [111]$ for a uniform M (refs 86,103,104). In accordance with the vortex-like M distribution of the skyrmion, a corresponding local P distribution is also expected, producing the polarization-density-wave-like feature in the SkX phase[103,104]. This local P distribution may also enable the manipulation of skyrmions in terms of electric field gradients[105,106].

As described in the section 'Observation of skyrmions in chiral-lattice magnets', the emergence of skyrmions is not restricted to the DM-interaction helimagnets but also occurs in centrosymmetric magnets in a thin-film form. In this case, the dipolar interaction plays a key role, together with the uniaxial magnetic anisotropy. Similar to the case of helimagnets, the striped phase is observed at low fields when the out-of-plane magnetic anisotropy exceeds some critical value to suppress the uniform in-plane M. On the other hand, the bubble lattice phase in such an anisotropic Heisenberg system may show a rich variety of bubble shapes due to the higher-order terms of the magnetic anisotropy as well as to the magnetic helicity degree of freedom.

We show some examples of the helimagnetic (including skyrmion) phases as observed by LTEM for the centrosymmetric magnet, $Ba(Fe_{1-x-0.05}Sc_xMg_{0.05})_{12}O_{19}$ ($x = 0.16$), hereafter referred to as BFSO (ref. 41). The parent compound $BaFe_{12}O_{19}$ (BFO) is a well-known hexaferrite, which is commercially produced in large quantities, with a magnetic transition temperature above 700 K and a magnetic easy-axis along the c axis. In a thin (~50 nm) c-plane film of BFSO, in which the magnetic anisotropy is controlled and slightly weakened by Sc doping, a highly disordered helimagnetic texture with frequent reversals of magnetic helicity is observed at room temperature and in zero magnetic field (Fig. 3a). When a magnetic field is applied normal to the film, the SkX phase emerges as shown by under-focused LTEM images (Fig. 3b,c); each skyrmion shows as either a black or a white circle-disk in a random manner, indicating that the skyrmion helicity (for example, clockwise or anticlockwise curl of the in-plane M) is not correlated, but disordered in this triangular-lattice of SkX. On increasing the field strength, the skyrmion size tends to decrease, while the SkX lattice constant increases (Fig. 3c). This is in contrast to the case of the nearly magnetic-field-independent shape of the SkX in the chiral-lattice DM magnet.

To scrutinize each skyrmion, its magnified picture based on the transport-of-intensity analysis is shown in Fig. 3d,e. The in-plane M curl (magnetic helicity) changes its direction (sign) twice in going from the peripheral to core regions, forming a triple-ring feature. When mapped on to the unit sphere, the local M shows a pendulum-like oscillation, as shown in Fig. 3f. Nevertheless, in total, the

change in M wraps around the total sphere only once, indicating $N_{sk} = 1$. In this way, the helicity degree of freedom allowed in the centrosymmetric magnet may greatly enrich the skyrmion features, as predicted also by simulations[41]. Note that the equation of motion for a skyrmion does not depend on the helicity but on the skyrmion number as described in the section 'Dynamics of skyrmions'.

Recently, a spontaneous atomic-scale magnetic skyrmion lattice has been discovered by spin-polarized scanning tunnelling microscopy in a hexagonal Fe film of one atomic layer on an Ir(111) surface[12]. The skyrmion lattice is incommensurate with the underlying atomic lattice. Theoretical analysis has concluded that the four-spin interaction, combined with the DM interaction, stabilizes the square skyrmion lattice even without an external magnetic field corresponding to cases (3) and (4) described earlier. An important issue to be addressed is how mobile this skyrmion crystal is, which is left for future studies.

An interesting question is 'Is there any possibility of stabilizing the skyrmion crystal without the spin–orbit or dipolar interactions being involved? A recent theory[39] answers this question affirmatively, which examined a frustrated classical spin model on a triangular lattice. With the frustration, the Fourier transform $J(\mathbf{q})$ of the exchange interaction $J_{ij} = J(\mathbf{R}_i - \mathbf{R}_j)$ between the two spins at sites $\mathbf{R}_i$ and $\mathbf{R}_j$ has maxima at several symmetrically equivalent momenta other than $\mathbf{q} = \mathbf{0}$. In the model[39], there are three momenta $\mathbf{Q}_1$, $\mathbf{Q}_2$, $\mathbf{Q}_3$ (and their opposite) giving the maxima, and correspondingly there are three possibilities, that is, single-$\mathbf{q}$ state, double-$\mathbf{q}$ state and triple-$\mathbf{q}$ state. The triple-$\mathbf{q}$ state corresponds to the skyrmion crystal state. The phase diagram in the T–B plane has been obtained; the skyrmion crystal state appears only at the finite T and B region, and an interesting Z state exists near the transition temperature. This Z state consists of domains of energetically degenerate skyrmions and anti-skyrmions states, which is a unique property of the skyrmion due to the frustrated exchange interaction discussed in the section 'Observation of skyrmions in chiral-lattice magnets'.

Topological phenomena related to skyrmions

The skyrmion structure as shown in Fig. 1a has a nontrivial geometrical aspect, that is, the non-coplanar spin configuration. This means that the spins form a solid angle, that is, scalar spin chirality, which is described by the gauge field a_μ introduced in Box 1 (here μ is the time–space index). The gauge field produces the electromagnetic field related to the spin configuration and is called EEMF; various topological phenomena are derived from this field[45–47], as schematically shown in Fig. 4a. The EEMF has geometrical meaning in spin space, and it generates physical effects when the spin structure is coupled to the conduction electrons. For simplicity let us assume that the conduction electron spin is coupled strongly to, and forced to be parallel to, the localized spin at each atomic site, that is, it obeys Hund's rule coupling. This constraint leads to the EEMF a_μ originating from the coupling of the spin textures to the conduction electrons (see Box 1). One remarkable consequence of this coupling is the spin-transfer torque effect as described in Box 1, and hence the combined equations of motion for the conduction electrons and the localized spins[52]

$$\frac{\partial f}{\partial t} + \mathbf{v} \cdot \nabla_r f - e\left[(\mathbf{E} + \mathbf{e}) + \mathbf{v} \times (\mathbf{B} + \mathbf{b})\right] \cdot \nabla_k f = -\frac{1}{\tau}(f - f_0) \quad (2)$$

$$\frac{\partial \mathbf{n}}{\partial t} + (\mathbf{j} \cdot \nabla)\mathbf{n} = -\mathbf{n} \times \frac{\delta H_S}{\delta \mathbf{n}} + \mathbf{n} \times \left[\alpha_G \frac{\partial \mathbf{n}}{\partial t} + \beta(\mathbf{j} \cdot \nabla)\mathbf{n}\right] \quad (3)$$

where equation (2) is the Boltzmann equation for the electron distribution function $f(\mathbf{r},\mathbf{k},t)$ at time t, and equation (3) is the Landau–Lifshitz–Gilbert equation for the spin. In equation (2), $\mathbf{E}(\mathbf{B})$ is the electric(magnetic) field, $\mathbf{e}(\mathbf{b})$ is the emergent electric(magnetic)

field, $\mathbf{k}$ is the wavevector, $\mathbf{v}$, τ, $-e$ and f_0 are the velocity, mean free time, charge and equilibrium distribution function of electrons, respectively. In equation (3), $\mathbf{j}$ is the current density of conduction electrons, H_S is the spin Hamiltonian, α_G the Gilbert damping constant and β represents the non-adiabatic effect[107–109]. Because of the Lorentz force $-e[(\mathbf{E} + \mathbf{e}) + \mathbf{v} \times (\mathbf{B} + \mathbf{b})]$ in equation (2), a Hall effect occurs due to $\mathbf{b}$, called the topological Hall effect (THE). In the SkX phase, the periodic array of the unit flux ($\phi_0 = h/e$, where h is the Planck constant) associated with each skyrmion leads to the almost uniform emergent magnetic field as

$$<b_z> = \frac{\sqrt{3}\phi_0}{2\lambda^2}$$

with $a_s = 2\lambda/\sqrt{3}$ being the lattice constant of the triangular skyrmion crystal.

As for the THE, there are already several experimental reports on MnSi (refs 48,49,51), FeGe (ref. 110) and MnGe (ref. 50). The first observation of the skyrmion-induced THE was in a narrow T–B window (Fig. 1b) of a MnSi bulk crystal, reporting the topological Hall resistivity ρ_H^T of about 5 nΩ cm. For MnSi with $\lambda = 18$ nm, $<b_z> = 11$ T (refs 49,51). In reality, the finite (non-unity) spin polarization (p) may lead to a reduction of the ρ_H^T magnitude, and by assuming $p \sim 0.22$ the observed value is consistent with the above rough estimate based on the normal Hall coefficient value and the skyrmion density[51]. Even before such an identification of the skyrmion-induced THE, a large additional Hall response was reported for a MnSi bulk crystal in a broader T–B region but under high pressures[48]; this may be reinterpreted in terms the THE characteristic of some new SkX form. Furthermore, recent transport experiments in bulk MnSi under pressure[64,65] strongly suggest the relevance of the skyrmions even without the formation of a skyrmion crystal.

The SkX phase region becomes more stable in thin films. To investigate this, THE measurements were done on thin films of FeGe (ref. 110) and MnSi (ref. 51); the SkX phase region in the B–T plane is identified by the magnitude of the THE response. Below, we discuss the case of a MnSi film with a thickness of 50 nm (ref. 51). The Hall resistivity can be expressed in general as $\rho_H = \rho_H^N + \rho_H^A + \rho_H^T = R_0 B + S_A \rho_{xx}^2 M + \rho_H^T$ where $\rho_H^N = R_0 B$ is the normal (Lorentz force) term where R_0 is the Hall coefficient, $\rho_H^A = S_A \rho_{xx}^2 M$ is the anomalous Hall resistivity induced by the spontaneous magnetization M through the spin–orbit interaction $\rho_{xx}^2 M$ (because the intrinsic anomalous Hall conductivity ($\sigma_H^A \sim \rho_H^A / \rho_{xx}^2$) is insensitive to scattering rate of the carrier or ρ_{xx} and hence proportional to M only), and the last term ρ_H^T represents the THE due to the scalar spin chirality. Without the THE, the B dependence of the Hall resistivity can be fitted well with the conventional two terms; conversely, the THE can be estimated as the deviation of the observed Hall resistivity from the fitted curve with the conventional terms. This procedure is demonstrated in Fig. 4c. The topological Hall resistivity ρ_H^T at 25 K (Fig. 4c) is about 8 nΩ cm, comparable with or slightly larger than the bulk value. As seen in the contour map of ρ_H^T, the expanded region of the SkX phase in the MnSi thin film can be deduced (Fig. 4d).

As an even more conspicuous example of the THE in the SkX phase, we show results of the Hall resistivity for a bulk polycrystal of B20-type cubic MnGe, which has a short helical pitch λ that changes from 3 nm to 6 nm with temperature[50]. The temperature-dependent change of λ indicates that there should be another important factor, which is likely to be the magnetic anisotropy, in addition to the competition between the ferromagnetic exchange and DM interactions. Reflecting this nature, the SkX feature seems to be qualitatively different from the conventional one, that is, the vertical magnetic field-induced hexagonal skyrmion lattice observed typically in chiral-lattice magnets. Recent SANS measurements indicate that the three-dimensional skyrmion lattice as shown schematically
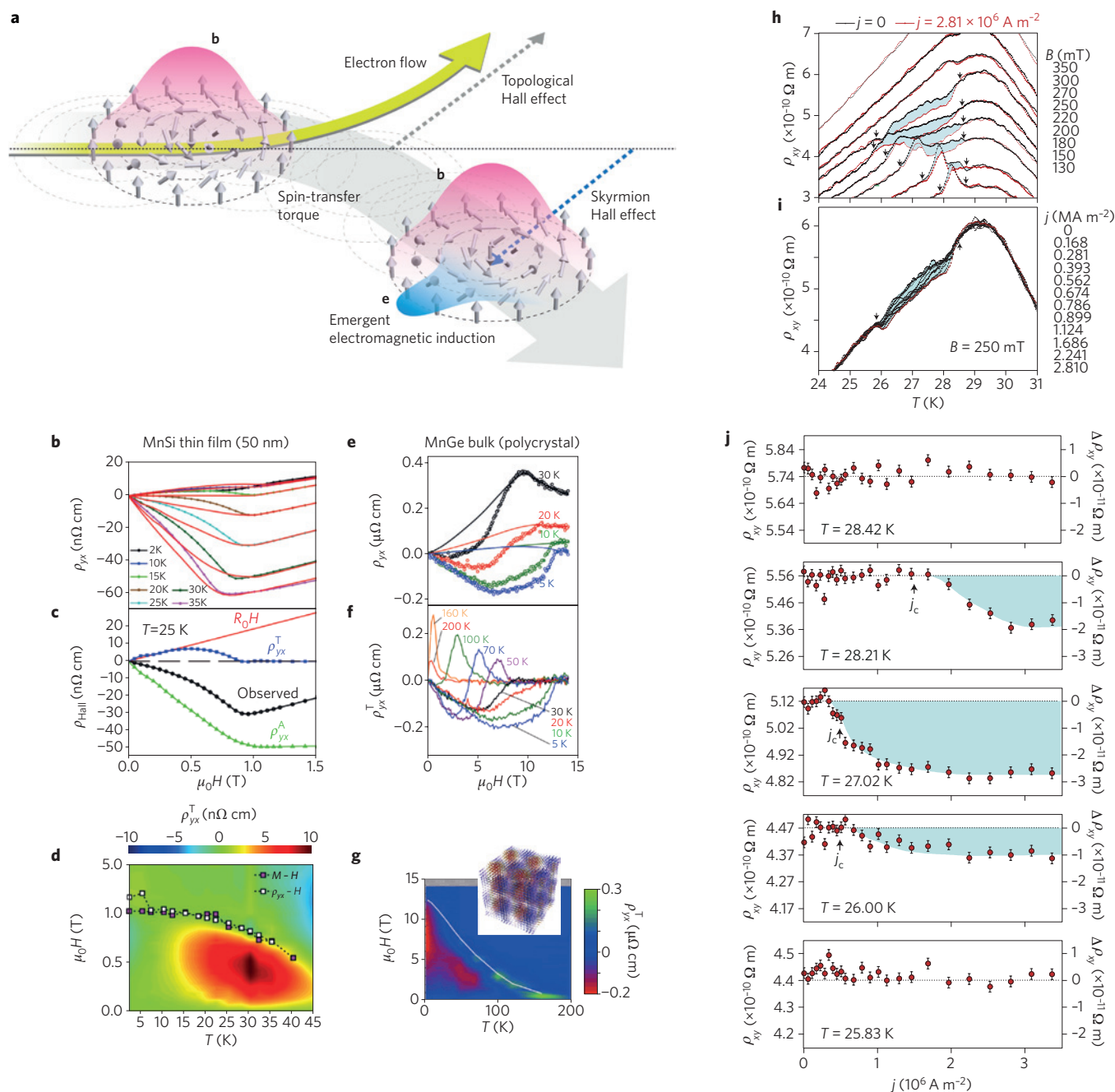
Figure 4 | Topological phenomena of skyrmions. a, Schematic picture of skyrmion motion and associated physical phenomena under the flow of electrons. Electron current drives the flow of a skyrmion by means of the spin-transfer torque mechanism. (Note that the direction of the charge current is the opposite to the electron flow.) Electrons are deflected by the Lorentz force due to the emergent magnetic field **b** of the skyrmion, which results in the THE. The velocity of the skyrmion has its transverse component proportional to α_G–β, that is, the skyrmion Hall effect. The motion of the skyrmion is accompanied by the time-dependent emergent magnetic field **b** (pink), and hence the emergent electric field **e**, that is, emergent electromagnetic induction. **b**–**g**, Experimental observation of the THE. **b**, Hall resistivity $\rho_H = \rho_{yx}$ in a MnSi thin film as a function of the magnetic field at various temperatures. **c**, The decomposition of the Hall resistivity to various contributions as $\rho_H = \rho_H^N + \rho_H^A + \rho_H^T = R_0 H + S_A \rho_{xx}^2 M + \rho_H^T$. **d**, Colour contour map of the magnitude of the topological contribution $\rho_H^T + \rho_{yx}^T$. **e**–**g**, Same as for **b**–**d**, except for a MnGe bulk sample. The inset of **g** is a model calculation of the three-dimensional skyrmion crystal. **h**–**j**, Experimental data for the current-driven emergent electromagnetic induction in bulk MnSi. **h**, Hall resistivity ρ_{yx} as a function of temperature for several magnetic field strengths. The black curves are for the limit of zero d.c. current density j, and the red are for $j = 2.81 \times 10^6$ A m^{-2}. Black arrows indicate the phase boundaries of the A phase, that is, skyrmion crystal state. It is noted that the Hall signal is suppressed in the skyrmion crystal phase due to the topological contribution (blue shaded region). **i**, Current density j dependence of the Hall resistivity in the skyrmion lattice phase of MnSi under a large applied d.c. electric current. Black arrows indicate the phase boundaries of the skyrmion crystal state. **j**, The change in the Hall resistivity ρ_{yx} as a function of j at $B = 250$ mT for several temperatures. The suppression of the signal above the threshold current density j_c, which corresponds to the onset of the skyrmion crystal motion, is observed. This can be understood by the emergent electric field that is generated by the temporal change of the emergent magnetic field associated with skyrmions, that is, emergent electromagnetic induction. The error bars represent the statistical error of the data after subtracting a spline fit[54]. Figure reproduced with permission from: **b**–**d**, ref. 51, © 2013 APS; **e**–**g**, ref. 50, © 2011 APS; **h**–**j**, ref. 54, © 2012 NPG.
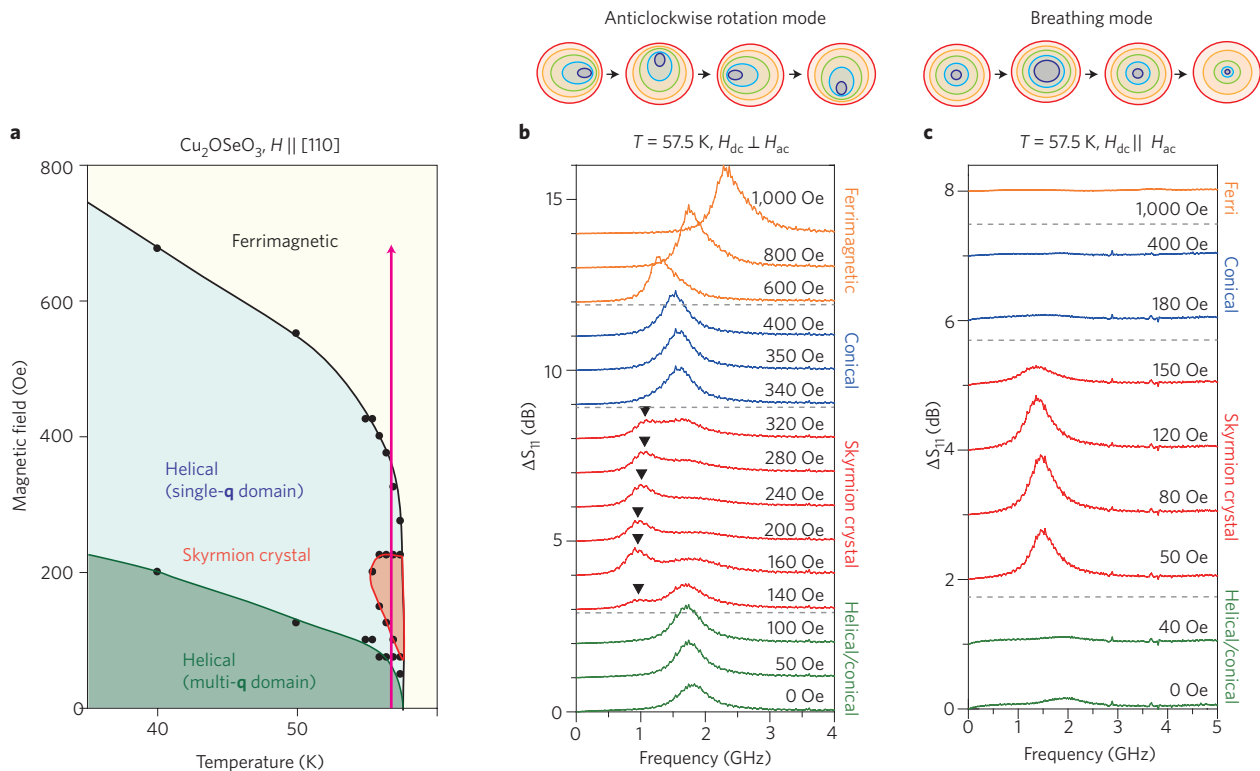
Figure 5 | Experimental data for skyrmion magnetic resonances in Cu$_2$OSeO$_3$. a, Magnetic phase diagram determined by the magnetic susceptibility. The vertical arrow indicates the magnetic field scan at $T = 57.5$ K. **b,c**, Microwave absorption spectra ΔS_{11} for the static magnetic field H_{dc} perpendicular to the a.c. magnetic field H_{ac} at various magnetic fields at $T = 57.5$ K. **c**, Similar plot to **b** for H_{dc} parallel to H_{ac}. The schematics at the top are of the corresponding collective modes. The colours indicate the normal component of the spins from positive (red) to negative (blue). The arrowheads show the time evolution profile of a skyrmion in its crystal phase. Figure reproduced with permission from ref. 125, © 2012 APS.

in the inset to Fig. 4g may be realized in the whole T–B region of the helimagnet[72]. At zero field, the compound shows no net magnetization and the SkX may be alternately composed of skyrmions and anti-skyrmions; this state may be viewed as the multiple-**q** state of the three <100> helices orthogonal to each other. An external magnetic field may induce a net magnetization and cause a non-zero scalar net spin chirality (skyrmion number), giving rise to the THE. The results of Hall resistivity for MnGe are shown in Fig. 4e and the extracted topological component in Fig. 4f (ref. 50). In the magnetization process, the topological Hall resistivity ρ_H^T reaches a maximum value of −200 nΩ cm, which appears nearly constant as long as λ (~3 nm) stays nearly constant below 70 K. This is a feature of the real-space EEMF **b** acting on the conduction electron, as in the case of the Lorentz-force Hall effect that is independent of temperature or electron scattering rate. The magnetic-field variations for ρ_H^T can be well accounted for by the cubic lattice of the SkX. The magnitude of p**b** is estimated to be ≈40 T. Thus, the THE of the high-density SkX can greatly enhance the action of the external magnetic field.

There are several theoretical issues studied besides the THE discussed above, such as the dynamics of the conduction electrons and spin system[111–113], and possible three-dimensional skyrmion crystals[114,115]. Also some experiments suggest the existence of the three-dimensional skyrmionic states[116,117].

Dynamics of skyrmions

The real advantage of skyrmions compared with other magnetic nanostructures lies in their peculiar dynamics especially when combined with the conduction electrons or electric polarization. Intensive interest has been triggered by the experimental discovery[43] of current-driven skyrmion crystal motion by an ultralow current density of the order of 10^6 A m^{-2}, which is five or six orders of magnitude smaller than that needed for domain wall motion in

ferromagnets. Recently, the current-driven motion of the skyrmion crystal in a thin film of FeGe has been studied by LTEM[44]. By comparing the motion of the helical and the skyrmion crystal phases, it was observed that a current density less than 10^6 A m^{-2} can drive the motion only in the latter case. This small critical current density enables the manipulation of information with low-power consumption per bit in the slow-speed regime. However, high-speed manipulation requires a similar current density to that for domain wall motion.

Equations (B4a) and (B4b) in Box 1 indicate that once the skyrmions move, an electric field is induced by the relation

$$\nabla \times \mathbf{e} = -\frac{\partial \mathbf{b}}{\partial t}$$

or more explicitly $\mathbf{e} = \mathbf{v}_d \times \mathbf{b}$, where $\mathbf{v}_d$ is the drift velocity of the skyrmion crystal. As a function of the current density j, $\mathbf{v}_d$ remains zero below a critical value j_c, and begins to increase for $j > j_c$. Correspondingly, the induced emergent electric field $\mathbf{e}$ gives a Hall effect in the opposite direction to the topological Hall effect[52] (Fig. 4h). Therefore, $\Delta\rho_{yx}$ as a function of j shows a characteristic behaviour, which is observed experimentally in MnSi (Fig. 4i,j)[54].

Theoretically, it is important to derive the equation for the motion of the centre of mass of a skyrmion. This can be achieved by the method originally proposed by Thiele and its generalization[107–109]. The results read[71]

$$M_S \frac{d\mathbf{v}_d}{dt} + \mathbf{G} \times (\mathbf{j} - \mathbf{v}_d) + \kappa\,(\alpha_G \mathbf{v}_d - \beta\mathbf{j}) = -\nabla U \qquad (4)$$

where $\mathbf{v}_d = d\mathbf{R}/dt = (\dot{X}, \dot{Y})$, $\mathbf{R} = ((X,Y)$ are the centre of mass coordinates), M_S is the mass of the skyrmion, κ is a dimensionless constant
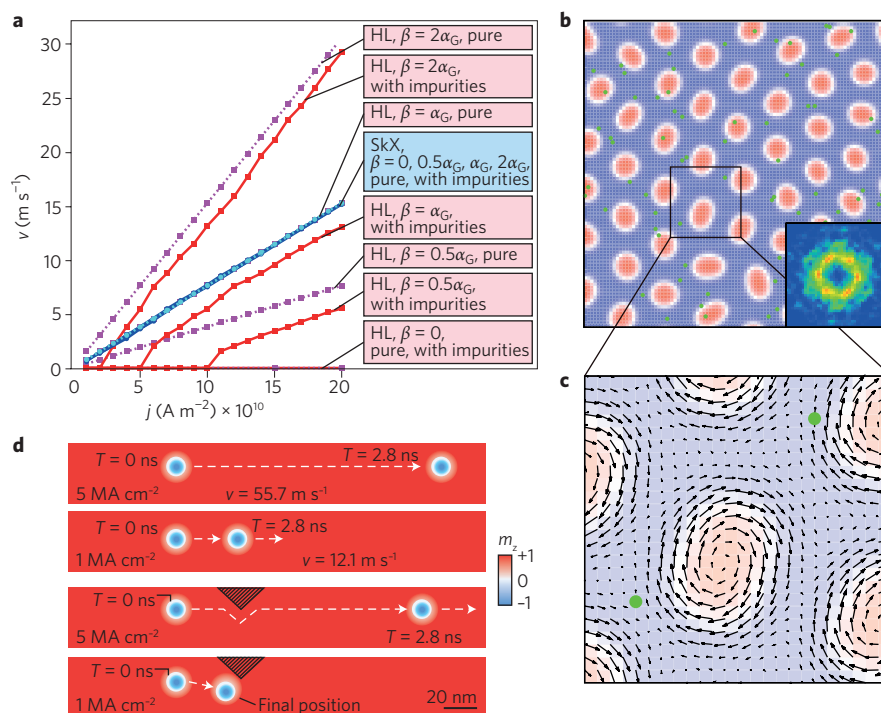
Figure 6 | Simulations of the skyrmion motion driven by current. a, Current–velocity (j–v) relation for the helix structure (HL) and skyrmion crystal (SkX) calculated by solving the Landau–Lifshitz–Gilbert equation numerically. The j–v characteristics for a skyrmion crystal (blue) are universal, and independent of α_G, β and the impurity pinning effect, while the j–v characteristics for the helical phase are sensitive to these factors (red and pink). **b,** Snapshot of the skyrmion crystal in motion and its Fourier transformation (inset). The green dots specify the position of impurities. **c,** Zoom-in view showing the deformation of an individual skyrmion as well as of the skyrmion lattice at motion. **d,** Motion of a skyrmion under the application of current in a stripe-shaped sample without (upper panels) and with (lower panels) a notch structure. Figure reproduced with permission from: **a–c**, ref. 122, © 2013 NPG; **d**, ref. 109, © 2013 NPG.

of the order of unity, and $\mathbf{G} = 2\pi N_{sk}\mathbf{e}_z$ (where $\mathbf{e}_z$ is the unit vector along the z direction) is the gyrovector. U is the potential for the skyrmion due to boundary effects, magnetic fields and impurities. The mass term in equation (4) comes from the deformation of the moving skyrmion compared with the static solution, and can be neglected in the low-frequency limit. Then, equation (4) indicates a canonical conjugate relation between X and Y. The velocity d$\mathbf{R}$/dt is perpendicular to the force or along the equal potential contour similar to the case of a charged particle in a magnetic field. It is straightforward to generalize this equation of motion to many skyrmions.

Because the skyrmion crystal breaks translational symmetry, there is a Goldstone mode, that is, a phonon of the skyrmion crystal. Note that rotational symmetry in spin space is broken by the external magnetic field, and hence the spin wave modes are gapped, and this phonon mode is the only gapless low-lying mode. It is predicted that there is only one phonon branch with dispersion $\omega_k \propto k^2$ (refs 52,118,119). It is noted here that the mass term has been suggested to play an important role in the dynamics of a skyrmion bounded in a circular disk as observed in numerical simulations[120,121].

Another prediction from equation (4) is the skyrmion Hall effect. In the presence of the Gilbert damping α_G and non-adiabatic effect β in the Landau–Lifshtz–Gilbert equation, there occurs a velocity $v_\perp = (\alpha_G - \beta)j$ transverse to the current $\mathbf{j}$ when higher-order terms in α_G and β are neglected[52,71,122–124].

The collective modes of the skyrmion crystal were experimentally studied by the magnetic resonance in insulating Cu_2OSeO_3 (ref. 125). In its bulk form, the SkX phase is confined within a rather narrow window of magnetic field (H_{dc}) and T as shown in Fig. 5a, contrary to the extended SkX region of its thin-film form. The SkX hexagonal lattice plane (referred to as the xy plane) is formed perpendicular to the H_{dc} direction (z). Then, we can define

the three $k = 0$ skyrmion 'optical' modes; namely, anticlockwise (ACW) rotation, clockwise (CW) rotation and breathing modes of the skyrmion core, as schematically shown in the top panels of Fig. 5b,c. When an alternating current (a.c) magnetic field (H_{ac}) of the microwaves is applied parallel to the skyrmion plane (that is, $H_{ac} \perp H_{dc}$), the former two rotational modes should be excited. In the SkX phase region denoted by the red curves in Fig. 5b, a skyrmion-related magnetic resonance at 1.0 GHz is observed (indicated by closed triangles), distinct from the magnetic resonances of the conical and ferromagnetic (spin collinear) states; this mode is assigned to the ACW motion mode of the skyrmion based on simulation results, although the higher-lying CW mode is not clearly distinguishable from the conical state magnetic resonance mode. The well-defined breathing mode of the skyrmion appears at 1.5 GHz in the configuration of $H_{ac} \parallel H_{dc}$ as shown in Fig. 5c, where no magnetic resonance is allowed for the other magnetic phases. The SkX phase also shows a ferroelectric polarization as described in the section 'Skyrmions in different magnetic systems', therefore all the modes are magnetoelectric in nature; they should be active also for a.c. electric-field excitation and hence are termed electromagnons. Such magnetically and electrically active skyrmion excitation modes are expected to show the optical magnetoelectric effect, such as the directional dichroism, that is, a distinct response depending on the direction of light propagation (microwave)[126,127].

Perspectives on 'skyrmionics'
From the viewpoint of applications skyrmions have several potential advantages compared with the domain walls in ferromagnets[107,108]. Both are subject to the spin-transfer torque effect, and can be driven by a spin-polarized current. However, even though the

equations of motion seem to be similar in the two cases, the physics are essentially different[122,123,124]. Namely, the equation of motion for the magnetic domain wall reads with constant current density

$$\alpha_G \dot{X} = \beta j_x - \frac{\partial U}{\partial X} \qquad (5)$$

which should be compared with equation (4). (Here M_S has been neglected assuming steady motion.) The essential difference comes from the fact that the emergent magnetic field b_z is finite for skyrmions, which gives the canonical conjugate relation between X and Y, whereas for a magnetic domain wall b_z is zero, and the tilting angle from the easy plane is the conjugate variable to X. Equation (5) yields the relation $\dot{X} = (\beta/\alpha_G)j_x$ without the pinning potential. Especially, when $\beta = 0$, there is no motion induced by the current j_x as long as it is smaller than a critical value. This is called intrinsic pinning. Considering that $\alpha_G, \beta << 1$, the pinning effect is enhanced compared with the case of skyrmion by a factor of $1/\beta$ ($>>1$) (refs 71,122).

Rosch et al.[71] introduced a phenomenological expression for the pinning force as $\mathbf{F}_{pin} = -4\pi M_S f(v_d/v_{pin})(\mathbf{v}_d/v_d)$ where f is a scaling function and v_{pin} is a velocity characterizing the strength of the pinning force. Iwasaki et al.[122,123] studied the current-driven motion of both the helical state and skyrmion crystal in a model with DM interaction taking into account the impurity pinning effect due to the easy-axis anisotropy. They observed a universal current–velocity relation for the skyrmion crystal almost independent of α_G, β and impurity pinning, in sharp contrast to the motion of the helical state that shows current–velocity relations similar to those of a magnetic domain wall[122,123] (Fig. 6a). The reduced critical current density for the skyrmion crystal was attributed to the deformation of the crystal and of individual skyrmions to avoid the impurity potential[122,128,129] (Fig. 6b,c). Note that this result comes from equation (4), which gives the motion of skyrmions transverse to the potential gradient. The pinning of skyrmions has some resemblance to that of vortices in superconductors[130]. The reduced critical current density could enable low-energy operation for future memory devices. In particular, the energy cost per unit time is proportional to the square of the current density, whereas it is inversely proportional to the time needed to manipulate a fixed amount of information. Therefore, the energy cost for a fixed amount of information is proportional to the current density. Skyrmion dynamics in constricted geometries are an important issue to consider, especially for applications. An example is shown in Fig. 6d where skyrmion motion in a finite-width geometry, and in the presence of a notch, has been simulated[109,123,124]. Sampaio et al. also studied the stability and nucleation of skyrmion in nanodiscs[124]. Further studies on this issue are highly desired[131,132]. Recently, nanowire samples of the B20 silicide phase have been fabricated[133], and the skyrmion lattice has been observed[134]. The dynamics of the generation of skyrmions is another important problem that remains to be explored[77,135–138].

Finally, we note that the dynamics of skyrmions are similar to that of merons, but there is an essential difference between the two, that is, the latter is not a local object[14,15]. The energy of a meron logarithmically diverges with the size of the sample; one needs to introduce a meron and anti-meron pair for an infinitely large sample. (A similar statement applies to magnetic vortices that have a singularity at the core.) We thus regard a skyrmion to be more useful as an information carrier because it is a stable and localized particle of finite size that is easily manipulated by current or electric field.

In summary, a skyrmion is a topologically stable particle observed in certain magnets, which has peculiar dynamics. Because skyrmions comprise many spins, thermal and quantum fluctuations are expected to be small, which is advantageous for memory applications[139]. There remain many intriguing and important issues to be addressed, such as the creation and annihilation processes,

formation of composite structures including merons, reversal of helicity, possible three-dimensional skyrmion structures[140], and the non-equilibrium phenomena under a current[141]. From an applications perspective, the nanoscale fabrication of samples is an important step, along with the design and demonstration of skyrmion logic circuits enabled by fundamental understanding of the basic physics of the skyrmions.

References

1. Skyrme, T. H. R. A unified field theory of mesons and baryons. *Nucl. Phys.* **31,** 556–569 (1962).
    This is the original paper that proposed the skyrmion as a model for hadrons.
2. Sondhi, S. L., Karlhede, A., Kivelson, S. A. & Rezayi, E. H. Skyrmions and the crossover from the integer to fractional quantum Hall effect at small Zeeman energies. *Phys. Rev. B* **47,** 16419–16426 (1993).
3. Wright, D. C. & Mermin, N. D. Crystalline liquids: the blue phases. *Rev. Mod. Phys.* **61,** 385–432 (1989).
4. Ho, T. L. Spinor Bose condensates in optical traps. *Phys. Rev. Lett.* **81,** 742–745 (1998).
5. Bogdanov, N. & Yablonskii, D. A. Thermodynamically stable "vortices" in magnetically ordered crystals. The mixed state of magnets. *Sov. Phys. JETP* **68,** 101–103 (1989).
6. Bogdanov, N. & Hubert, A. Thermodynamically stable magnetic vortex states in magnetic crystals. *J. Magn. Magn. Mater.* **138,** 255–269 (1994).
7. Rößler, U. K., Bogdanov, N. & Pfleiderer, C. Spontaneous skyrmion ground states in magnetic metals. *Nature* **442,** 797–801 (2006).
    This is an early theoretical work predicting the formation of skyrmions in a magnetic system.
8. Binz, B., Vishwanath, A. & Aji, V. Theory of the helical spin crystal: A candidate for the partially ordered state of MnSi. *Phys. Rev. Lett.* **96,** 207202 (2006).
9. Tewari, S., Belitz, D. & Kirkpatrick, T. R. Blue quantum fog: Chiral condensation in quantum helimagnets. *Phys. Rev. Lett.* **96,** 047207 (2006).
10. Mühlbauer, S. *et al.* Skyrmion lattice in a chiral magnet. *Science* **323,** 915–919 (2009).
    This is the first experimental report on neutron scattering that identifies the A phase in a chiral magnet as the skyrmion crystal phase.
11. Yu, X. Z. *et al.* Real-space observation of a two-dimensional skyrmion crystal. *Nature* **465,** 901–904 (2010).
    This paper reports the first real-space observation of a skyrmion crystal and individual skyrmions by using Lorentz microscopy.
12. Heinze, S. *et al.* Spontaneous atomic-scale magnetic skyrmion lattice in two dimensions. *Nature Phys.* **7,** 713–718 (2011).
    This paper reports a spin-resolved STM study and theoretical analysis on the skyrmion crystal state at the interface.
13. Pfleiderer, C. Surfaces get hairy. *Nature Phys.* **7,** 673–674 (2011).
14. Rajaraman, R. *Solitons and Instantons* (Elsevier, 1987).
15. Braun, H.-B. Topological effects in nanomagnetism: From superparamagnetism to chiral quantum solitons. *Adv. Phys.* **61,** 1–116 (2012).
16. Tanygin, B. M. Symmetry theory of the flexomagnetoelectric interaction in the magnetic vortices and skyrmions. *Physica B* **407,** 868–872 (2012).
17. Lin, Y. S., Grundy, J. & Giess, E. A. Bubble domains in magnetostatically coupled garnet films. *Appl. Phys. Lett.* **23,** 485–487 (1973).
18. Malozemoff, A. P. & Slonczewski, J. C. *Magnetic Domain Walls in Bubble Materials* 306–314 (Academic, 1979).
19. Garel, T. & Doniach, S. Phase transitions with spontaneous modulation - the dipolar Ising ferromagnet. *Phys. Rev. B* **26,** 325–329 (1982).
20. Suzuki, T. A study of magnetization distribution of submicron bubbles in sputtered Ho-Co thin films. *J. Magn. Magn. Mater.* **31–34,** 1009–1010 (1983).
21. Dzyaloshinskii, I. A thermodynamic theory of "weak" ferromagnetism of antiferromagnetics. *J. Phys. Chem. Solids* **4,** 241–255 (1958).
22. Moriya, T. Anisotropic superexchange interaction and weak ferromagnetism. *Phys. Rev.* **120,** 91–98 (1960).
23. Ishikawa, Y., Tajima, K., Bloch, D. & Roth, M. Helical spin structure in manganese silicide MnSi. *Solid State Commun.* **19,** 525–528 (1976).
24. Ishikawa, Y. & Arai, M. Magnetic phase diagram of MnSi near critical temperature studied by neutron small angle scattering. *J. Phys. Soc. Jpn* **53,** 2726–2733 (1984).
25. Grigoriev, S. V. *et al.* Helical spin structure of Mn$_{1-y}$Fe$_y$Si under a magnetic field: Small angle neutron diffraction study. *Phys. Rev. B* **79,** 144417 (2009).
26. Lebech, B. *et al.* Magnetic phase diagram of MnSi. *J. Magn. Magn. Mater.* **140–144,** 119–120 (1995).

27. Pfleiderer, C. *et al.* Partial order in the non-Fermi-liquid phase of MnSi. *Nature* **427,** 227–231 (2004).

28. Janoschek, M. *et al.* Fluctuation-induced first-order phase transition in Dzyaloshinskii-Moriya helimagnets. *Phys. Rev. B* **87,** 134407 (2013).

29. Beille, J., Voiron, J. & Roth. M. Long period helimagnetism in the cubic B20 $Fe_xCo_{1-x}Si$ and $Co_xMn_{1-x}Si$ alloys. *Solid State Commun.* **47,** 399–402 (1983).

30. Ishimoto, K. *et al.* Small-angle neutron diffraction from the helical magnet $Fe_{0.8}Co_{0.2}Si$. *Physica B* **213–214,** 381–383 (1995).

31. Grigoriev, S. V. *et al.* Magnetic structure of $Fe_{1-x}Co_xSi$ in a magnetic field studied via small-angle polarized neutron diffraction. *Phys. Rev. B* **76,** 224424 (2007).

32. Grigoriev, S. V. *et al.* Crystal handedness and spin helix chirality in $Fe_{1-x}Co_xSi$. *Phys. Rev. Lett.* **102,** 037204 (2009).

33. Onose, Y., Takeshita, N., Terakura, C., Takagi, H. & Tokura, Y. Doping dependence of transport properties in $Fe_{1-x}Co_xSi$. *Phys. Rev. B* **72,** 224431 (2006).

34. Lebech, B., Bernhard, J. & Freltoft, T. Magnetic-structures of cubic FeGe studied by small-angle neutron scattering. *J. Phys. Condens. Matter* **1,** 6105–6122 (1989).

35. Uchida, M. *et al.* Topological spin textures in the helimagnet FeGe. *Phys. Rev. B* **77,** 184402 (2008).

36. Yu, X. Z. *et al.* Near room-temperature formation of a skyrmion crystal in thin-films of the helimagnet FeGe. *Nature Mater.* **10,** 106–109 (2011).

37. Wilhelm, H. Precursor phenomena at the magnetic ordering of the cubic helimagnet FeGe. *Phys. Rev. Lett.* **107,** 127203 (2011).

38. Shibata, K. *et al.* Towards control of the size and helicity of skyrmions in helimagnetic alloys by spin–orbit coupling. *Nature Nanotech.* **8,** 723–728 (2013).

39. Okubo, T., Chung, S. & Kawamura, H. Multiple-q states and the skyrmion lattice of the triangular-lattice heisenberg antiferromagnet under magnetic fields. *Phys. Rev. Lett.* **108,** 017206 (2012).

40. Bader, S. D. Colloquium: Opportunities in nanomagnetism. *Rev. Mod. Phys.* **78,** 1–15 (2006).

41. Yu, X. Z. *et al.* Magnetic stripes and skyrmions with helicity reversals. *Proc. Natl Acad. Sci. USA* **109,** 8856–8860 (2012).

42. Rosch, A. Extra twist in magnetic bubbles. *Proc. Natl Acad. Sci. USA* **109,** 8793–8794 (2012).

43. Jonietz, F. *et al.* Spin transfer torques in MnSi at ultralow current densities. *Science* **330,** 1648–1651 (2010).
This paper demonstrates the ultralow critical current density required for the current-driven motion of a skyrmion crystal.

44. Yu, X. Z. *et al.* Skyrmion flow near room temperature in an ultralow current density. *Nature Commun.* **3,** 988 (2012).

45. Volovik, G. *The Universe in a Helium Droplet* (Oxford Univ. Press, 2003).

46. Nagaosa, N. & Tokura, Y. Emergent electromagnetism in solids. *Physica Scripta* **T146,** 014020 (2012).

47. Nagaosa, N., Yu, X. Z. & Tokura, Y. Gauge fields in real and momentum spaces in magnets: monopoles and skyrmions. *Phil. Trans. R. Soc. A* **370,** 5806–5819 (2012).

48. Lee, M., Kang, W., Onose, Y., Tokura, Y. & Ong, N. P. Unusual Hall anomaly in MnSi under pressure. *Phys. Rev. Lett.* **102,** 186601 (2009).

49. Neubauer, A. *et al.* Topological Hall effect in the A phase of MnSi. *Phys. Rev. Lett.* **102,** 186602 (2009).

50. Kanazawa, N. *et al.* Large topological Hall effect in a short-period helimagnet MnGe. *Phys. Rev. Lett.* **106,** 156603 (2011).

51. Yufan Li, Y. *et al.* Robust formation of skyrmions and topological Hall effect anomaly in epitaxial thin films of MnSi. *Phys. Rev. Lett.* **110,** 117202 (2013).

52. Zang, J., Mostovoy, M., Han, J. H. & Nagaosa, N. Dynamics of skyrmion crystals in metallic thin films. *Phys. Rev. Lett.* **107,** 136804 (2011).

53. Van Hoogdalem, K. A., Tserkovnyak, Y. & Loss, D. Magnetic texture-induced thermal Hall effects. *Phys. Rev. B* **87,** 024402 (2013).

54. Schulz, T. *et al.* Emergent electrodynamics of skyrmions in a chiral magnet. *Nature Phys.* **8,** 301–304 (2012).
This paper demonstrates the electromagnetic induction generated by the emergent electromagnetic field.

55. Bak, P. & Jensen, M. H. Theory of helical magnetic structures and phase transitions in MnSi and FeGe, *J. Phys. C* **13,** L881–L885 (1980).

56. Landau, L. D., Lifshitz, E. M. & Pitaevskii, L. P. *Electrodynamics of Continuous Media* Vol. 8, Ch. 5, 178–179 (Elsevier, 2008).

57. Bloch, D., Voiron, J., Jaccarino, V. & Wernick, J. H. The high field–high pressure magnetic properties of MnSi. *Phys. Lett. A* **51,** 259–261 (1975).

58. Pfleiderer, C. *et al.* Magnetic quantum phase transition in MnSi under hydrostatic pressure. *Phys. Rev. B* **55,** 8330–8338 (1997).

59. Pfleiderer, C. *et al.* Non-Fermi-liquid nature of the normal state of itinerant-electron ferromagnets. *Nature* **414,** 427–430 (2001).

60. Doiron-Leyraud, N. *et al.* Fermi-liquid breakdown in the paramagnetic phase of a pure metal. *Nature* **425,** 595–599 (2003).

61. Pfleiderer, C., Boeni, P., Keller, T., Roessler, U. K. & Rosch, A. Non-Fermi liquid metal without quantum criticality. *Science* **316,** 1871–1874 (2007).

62. Hamann, A. *et al.* Magnetic blue phase in the chiral itinerant magnet MnSi. *Phys. Rev. Lett.* **107,** 037207 (2011).

63. Pappas, C. *et al.* Magnetic fluctuations and correlations in MnSi: Evidence for a chiral skyrmion spin liquid phase. *Phys. Rev. B* **83,** 224405 (2011).

64. Ritz, R. *et al.* Formation of a topological non-Fermi liquid in MnSi. *Nature* **497,** 231–234 (2013).

65. Ritz, R. *et al.* Giant generic topological Hall resistivity of MnSi under pressure. *Phys. Rev. B* **87,** 134424 (2013).

66. Kadowaki, K., Okuda, K. & Date, M. Magnetization and magnetoresistance of MnSi. I. *J. Phys. Soc. Jpn* **51,** 2433–2438 (1982).

67. Pleiderer, C. *et al.* Skyrmion lattices in metallic and semiconducting B20 transition metal compounds. *J. Phys. Condens. Matter* **22,** 164207 (2010).

68. Muenzer, W. *et al.* Skyrmion lattice in the doped semiconductor $Fe_{1-x}Co_xSi$. *Phys. Rev. B* **81,** 041203 (2010).

69. Seki, S. *et al.* Formation and rotation of skyrmion crystal in the chiral-lattice insulator Cu_2OSeO_3. *Phys. Rev. B* **85,** 220406 (2012).

70. Moskvin, E. *et al.* Complex chiral modulations in FeGe close to magnetic ordering. *Phys. Rev. Lett.* **110,** 077207 (2013).

71. Everschor, K. *et al.* Rotating skyrmion lattices by spin torques and field or temperature gradients. *Phys. Rev. B* **86,** 054432 (2012).

72. Kanazawa, N. *et al.* Possible skyrmion-lattice ground state in the B20 chiral-lattice magnet MnGe as seen via small-angle neutron scattering. *Phys. Rev. B* **86,** 134425 (2012).

73. Adams, T. *et al.* Long-range crystalline nature of the skyrmion lattice in MnSi. *Phys. Rev. Lett.* **107,** 217206 (2011).

74. Moskvin, E. *et al.* Complex chiral modulations in FeGe close to magnetic ordering. *Phys. Rev. Lett.* **110,** 077207 (2013).

75. Bauer, A., Garst, M. & Pfleiderer, C. Specific heat of the skyrmion lattice phase and field-induced tricritical point in MnSi. *Phys. Rev. Lett.* **110,** 177207 (2013).

76. Adams, T. *et al.* Long-wavelength helimagnetic order and skyrmion lattice phase in Cu_2OSeO_3. *Phys. Rev. Lett.* **108,** 237204 (2012).

77. Milde, P. *et al.* Unwinding of a skyrmion lattice by magnetic monopoles. *Science* **340,** 1076–1080 (2013).

78. Heinze, S. *et al.* Real-space imaging of two-dimensional antiferromagnetism on the atomic scale. *Science* **288,** 1805–1808 (2000).

79. Khajetoorians, A. A. *et al.* Current-driven spin dynamics of artificially constructed quantum magnets. *Science* **339,** 55–59 (2013).

80. Freeman, M. R. & Choi, B. C. Advances in magnetic microscopy. *Science* **294,** 1484–1488 (2001).

81. Grundy, P. J. & Herd, S. R. Lorentz microscopy of bubble domains and changes in domain wall state in hexaferrites. *Phys. Stat. Sol. A.* **20,** 295–307 (1973).

82. Grundy, P. J. & Tebble, R. S. Lorentz electron microscopy. *Adv. Phys.* **17,** 153–242 (1968).

83. Ishizuka, K. & Allman, B. Phase measurement of atomic resolution image using transport of intensity equation. *J. Electron Microsc.* **54,** 191–197 (2005).

84. Uchida, M., Onose, Y., Matsui, Y. & Tokura, Y. Real-space observation of helical spin order. *Science* **311,** 359–361 (2006).

85. Tonomura, A. *et al.* Real-space observation of skyrmion lattice in helimagnet MnSi thin samples. *Nano Lett.* **12,** 1673–1677 (2012).

86. Seki, S., Yu, X. Z., Ishiwata, S. & Tokura, Y. Observation of skyrmions in a multiferroic material. *Science* **336,** 198–201 (2012).
This paper describes the discovery of a skyrmion crystal state and multiferroic behaviour in an insulating magnet.

87. Yi, S. D., Onoda, S., Nagaosa, N. & Han, J. H. Skyrmions and anomalous Hall effect in a Dyialoshinskii-Moriya spiral magnet. *Phys. Rev. B* **80,** 054416 (2009).

88. Han, J. H. *et al.* Skyrmion lattice in a two-dimensional chiral magnet. *Phys. Rev. B* **82,** 094429 (2010).

89. Li, Y.-Q., Liu, Y.-H. & Zhou, Y. General spin-order theory via gauge Landau-Lifshitz equation. *Phys. Rev. B* **84,** 205123 (2011).

90. Kiselev, N. S., Bogdanov, A. N., Schäfer, R. & Rößler, U. K. Chiral skyrmions in thin magnetic films: new objects for magnetic storage technologies? *J. Phys. D* **44,** 392001 (2011).

91. Butenko, A. B., Leonov, A. A., Rößler, U. K. & Bogdanov, A. N. Stabilization of skyrmion textures by uniaxial distortions in noncentrosymmetric cubic helimagnets. *Phys. Rev. B* **82,** 052403 (2010).

92. Wilson, M. N. *et al.* Extended elliptic skyrmion gratings in epitaxial MnSi thin films. *Phys. Rev. B* **86,** 144420 (2012).

93. Karhu, E. A. *et al.* Chiral modulations and reorientation effects in MnSi thin films. *Phys. Rev. B* **85,** 094429 (2012).

94. Rybakov, F. N., Borisov, A. B. & Bogdanov, A. N. Three-dimensional skyrmion states in thin films of cubic helimagnets. *Phys. Rev. B* **87,** 094424 (2013).

95. Kwon, H. Y. *et al.* Effect of anisotropy and dipole interaction on long-range order magnetic structures generated by Dzyaloshinskii-Moriya interaction. *J. Magn. Magn. Mater.* **324,** 2171–2176 (2012).

96. Morikawa, D., Shibata, K., Kanazawa, N., Yu, X. Z. & Tokura, Y. Crystal chirality and skyrmion helicity in MnSi and (Fe,Co)Si as determined by transmission electron microscopy. *Phys. Rev. B* **88,** 024408 (2013).

97. Bos, J.-W. G., Colin, C. V. & Palstra, T. T. M. Magnetoelectric coupling in the cubic ferrimagnet Cu$_2$OSeO$_3$. *Phys. Rev. B* **78,** 094416 (2008).

98. Fiebig, M. Revival of the magnetoelectric effect. *J. Phys. D* **38,** R123–R152 (2005).

99. Tokura, Y. Materials science - Multiferroics as quantum electromagnets. *Science* **312,** 1481–1482 (2006).

100. Cheong, S.-W. & Mostovoy, M. Multiferroics: a magnetic twist for ferroelectricity. *Nature Mater.* **6,** 13–20 (2007).

101. Katsura, H., Balatsky, A. V. & Nagaosa, N. Spin current and magnetoelectric effect in noncollinear magnets. *Phys. Rev. Lett.* **95,** 057205 (2005).

102. Jia, C., Onoda, S., Nagaosa, N. & Han, J. H. Microscopic theory of spin-polarization coupling in multiferroic transition metal oxides. *Phys. Rev. B* **76,** 144424 (2007).

103. Seki, S., Ishiwata, S. & Tokura, Y. Magnetoelectric nature of skyrmions in a chiral magnetic insulator Cu$_2$OSeO$_3$. *Phys. Rev. B* **86,** 060403 (2012).

104. Belesi, M. *et al.* Magnetoelectric effects in single crystals of the cubic ferrimagnetic helimagnet Cu$_2$OSeO$_3$. *Phys. Rev. B* **85,** 224413 (2012).

105. White, J. S. *et al.* Electric field control of the skyrmion lattice in Cu$_2$OSeO$_3$. *J. Phys. Condens. Matter* **24,** 432201 (2012).

106. Liu, Y.-H., Li, Y.-Q. & Hoon, H. J. Skyrmion dynamics in multiferroic insulators. *Phys. Rev. B* **87,** 100402 (2013).

107. Ono, T. in *Spin Current* (eds Maekawa, S., Valenzuela, S. O., Saitoh, E. & Kimura, T.) 402–423 (Oxford Univ. Press, 2012).

108. Thiaville, A., Nakatani, Y., Miltat, J. & Suzuki, Y. Micromagnetic understanding of current-driven domain wall motion in patterned nanowires. *Europhys. Lett.* **69,** 990–996 (2005).

109. Fert, A., Cros, V. & Sampaio, J. Skyrmions on the track. *Nature Nanotech.* **8,** 152–156 (2013).

110. Huang, S. X. & Chien, C. L. Extended skyrmion phase in epitaxial FeGe(111) thin films. *Phys. Rev. Lett.* **108,** 267201 (2012).

111. Ho, K-y., Kirkpatrick, T. R., Sang, Y. & Belitz, D. Ordered phases of itinerant Dzyaloshinsky-Moriya magnets and their electronic properties. *Phys. Rev. B* **82,** 134427 (2010).

112. Kirkpatrick, T. R. & Belitz, D. Columnar fluctuations as a source of non-Fermi-liquid behavior in weak metallic magnets. *Phys. Rev. Lett.* **104,** 256404 (2010).

113. Belitz, D. & Kirkpatrick, T. R. Quantum electrodynamics and the origins of the exchange, dipole-dipole, and Dzyaloshinsky-Moriya interactions in itinerant fermion systems. *Phys. Rev. B* **81,** 184419 (2010).

114. Binz, B. & Vishwanath, A. Theory of helical spin crystals: Phases, textures, and properties. *Phys. Rev. B* **74,** 214408 (2006).

115. Park, J.-H. & Han, J. H., Zero-temperature phases for chiral magnets in three dimensions. *Phys. Rev. B* **83,** 184406 (2011).

116. Ishiwata, S. *et al.* Versatile helimagnetic phases under magnetic fields in cubic perovskite SrFeO$_3$. *Phys. Rev. B* **84,** 054427 (2011).

117. Long, Y. W. *et al.* Evolution of magnetic phases in single crystals of SrFe$_{1-x}$Co$_x$O$_3$ solid solution. *Phys. Rev. B* **86,** 064436 (2012).

118. Mochizuki, M. Spin-wave modes and their intense excitation effects in skyrmion crystals. *Phys. Rev. Lett.* **108,** 017601 (2012).

119. Petrova, O. & Tchernyshyov, O. Spin waves in a skyrmion crystal. *Phys. Rev. B* **84,** 214433 (2011).

120. Moutafis, C., Komineas, S. & Bland, J. A. C. Dynamics and switching processes for magnetic bubbles in nanoelements. *Phys. Rev. B* **79,** 224429 (2009).

121. Makhfudz, I., Krueger, B. & Tchernyshyov, O. Inertia and chiral edge modes of a skyrmion magnetic bubble. *Phys. Rev. Lett.* **109,** 217201 (2012).

122. Iwasaki, J. Mochizuki, M. & Nagaosa, N. Universal current–velocity relation of skyrmion motion in chiral magnets. *Nature Commun.* **4,** 1463 (2013).

123. Iwasaki, J., Mochizuki, M. & Nagaosa, N. Electric-current-induced skyrmion dynamics in constricted geometries. *Nature Nanotech.* **8,** 742–747 (2013).

124. Sampaio, J., Cros, V., Rohart, S., Thiaville, A. & Fert, A. Nucleation, stability and current-induced motion of isolated magnetic skyrmions in nanostructures. *Nature Nanotech.* **8,** 839–844 (2013).

125. Onose, Y., Okamura, Y., Seki, S., Ishiwata, S. & Tokura, Y. Observation of magnetic excitations of skyrmion crystal in a helimagnetic insulator Cu$_2$OSeO$_3$. *Phys. Rev. Lett.* **109,** 037603 (2012).

126. Mochizuki, M. & Seki, S. Magnetoelectric resonances and predicted microwave diode effect of the skyrmion crystal in a multiferroic chiral-lattice magnet. *Phys. Rev. B* **87,** 134403 (2013).

127. Okamura, Y. *et al.* Microwave magnetoelectric effect via skyrmion resonance modes in a helimagnetic multiferroic. *Nature Commun.* **4,** 2391 (2013).

128. Liu, Y.-H. & Li, Y.-Q. A mechanism to pin skyrmions in chiral magnets. *J. Phys. Condens. Matter* **25,** 076005 (2013).

129. Rosch, A. Moving with the current. *Nature Nanotech.* **8,** 160–161 (2013).

130. Blatter, G., Feigel'man, M. V., Geshkenbein, V. B. & Larkin, A. I. Vortices in high-temperature superconductors. *Rev. Mod. Phys.* **66,** 1125–1388 (1994).

131. Du, H. *et al.* Magnetic vortex with skyrmionic core in a thin nanodisk of chiral magnets. *EPL* **101,** 37001 (2013).

132. Du, H. *et al.* Field-driven evolution of chiral spin textures in a thin helimagnet nanodisk. *Phys. Rev. B* **87,** 014401 (2013).

133. Schmitt, A. L., Higgins, J. M., Szczech, J. R. & Jin, S. Synthesis and applications of metal silicide nanowires. *J. Mater. Chem.* **20,** 223–235 (2010).

134. Yu, X. Z. *et al.* Observation of the magnetic skyrmion lattice in a MnSi nanowire by Lorentz TEM. *Nano Lett.* **13,** 3755–3759 (2013).

135. Ogasawara, T., Iwata, N., Murakami, Y., Okamoto, H. & Tokura, Y. Submicron-scale spatial feature of ultrafast photoinduced magnetization reversal in TbFeCo thin film. *Appl. Phys. Lett.* **94,** 162507 (2009).

136. Finazzi, M. *et al.* Laser-induced magnetic nanostructures with tunable topological properties. *Phys. Rev. Lett.* **110,** 177205 (2013).

137. Sun, L. *et al.* Creating an artificial two-dimensional skyrmion crystal by nanopatterning. *Phys. Rev. Lett.* **110,** 167201 (2013).

138. Tchoe, Y. & Han, J. H. Skyrmion generation by current. *Phys. Rev. B* **85,** 174416 (2012).

139. Felser, C. Skyrmions. *Angew. Chem. Int. Ed.* **52,** 1631–1634 (2013).

140. Ezawa, M. Compact merons and skyrmions in thin chiral magnetic films. *Phys. Rev. B* **83,** 100408 (2011).

141. Lin, S.-Z., Reichhardt, C., Batista, C. D. & Saxena, A. Driven skyrmions and dynamical transitions in chiral magnets. *Phys. Rev. Lett.* **110,** 207202 (2013).

Acknowledgements

Additional information

Reprints and permissions information is available online at www.nature.com/reprints. Correspondence should be addressed to N.N.

Competing financial interests

The authors declare no competing financial interests.